drones

Article

Operational Mapping of Salinization Areas in Agricultural Fields Using Machine Learning Models Based on Low-Altitude Multispectral Images

Ravil Mukhamediev [1,2], Yedilkhan Amirgaliyev [2], Yan Kuchin [2], Margulan Aubakirov [3], Alexei Terekhov [2], Timur Merembayev [2], Marina Yelis [1,2], Elena Zaitseva [4], Vitaly Levashenko [4], Yelena Popova [5], Adilkhan Symagulov [1,2,*] and Laila Tabynbayeva [6]

1 Institute of Automation and Information Technology, Satbayev University (KazNRTU), Satpayev Str., 22A, Almaty 050013, Kazakhstan; ravil.muhamedyev@gmail.com (R.M.)
2 Institute of Information and Computational Technologies, Pushkin Str., 125, Almaty 050010, Kazakhstan
3 Department of Information Technology, Maharishi International University, Fairfield, IA 52557, USA
4 Faculty of Management Science and Informatics, University of Zilina, Univerzitná 8215/1, 010 26 Žilina, Slovakia
5 Baltic International Academy, Lomonosov Str. 1/4, LV-1019 Riga, Latvia
6 LLP Kazakh Research Institute of Agriculture and Plant Growing, Almaty 040909, Kazakhstan
* Correspondence: asmogulove00@gmail.com

Abstract: Salinization of cultivated soil is an important negative factor that reduces crop yields. Obtaining accurate and timely data on the salinity of soil horizons allows for planning the agrotechnical measures to reduce this negative impact. The method of soil salinity mapping of the 0–30 cm layer on irrigated arable land with the help of multispectral data received from the UAV is described in this article. The research was carried out in the south of the Almaty region of Kazakhstan. In May 2022, 80 soil samples were taken from the ground survey, and overflight of two adjacent fields was performed. The flight was carried out using a UAV equipped with a multispectral camera. The data preprocessing method is proposed herein, and several machine learning algorithms are compared (XGBoost, LightGBM, random forest, support vector machines, ridge regression, elastic net, etc.). Machine learning methods provided regression reconstruction to predict the electrical conductivity of the 0–30 cm soil layer based on an optimized list of spectral indices. The XGB regressor model showed the best quality results: the coefficient of determination was 0.701, the mean-squared error was 0.508, and the mean absolute error was 0.514. A comparison with the results obtained based on Landsat 8 data using a similar model was performed. Soil salinity mapping using UAVs provides much better spatial detailing than satellite data and has the possibility of an arbitrary selection of the survey time, less dependence on the conditions of cloud cover, and a comparable degree of accuracy of estimates.

Keywords: soil salinity; unmanned aerial vehicle; spectral indexes; machine learning; XGBoost; LightGBM; random forest; support vector machines; ridge regression; elastic net

check for updates

Citation: Mukhamediev, R.; Amirgaliyev, Y.; Kuchin, Y.; Aubakirov, M.; Terekhov, A.; Merembayev, T.; Yelis, M.; Zaitseva, E.; Levashenko, V.; Popova, Y.; et al. Operational Mapping of Salinization Areas in Agricultural Fields Using Machine Learning Models Based on Low-Altitude Multispectral Images. *Drones* **2023**, *7*, 357. https://doi.org/10.3390/drones7060357

Academic Editor: Fei Liu

Received: 5 May 2023
Revised: 23 May 2023
Accepted: 25 May 2023
Published: 29 May 2023

1. Introduction

Soil salinity is the most important factor reducing the productivity of agricultural production. The paper [1] concludes that salinization covers up to 20% of the world irrigated lands' stock. Moreover, according to the data of [2], for the last 30 years, the amount of land exposed to salinization has increased by 2.4 times. Climate change and anthropogenic factors causing a sharp increase in the use of soil and water resources lead to increased salinity and land degradation, especially in arid regions [3]. The lands of Central Asia, including southern Kazakhstan, are clear examples of such negative changes [4], associated with reduced availability of irrigation water and adverse environmental conditions. For example, in Kyzylorda region of Kazakhstan, almost 85% (20.3 million ha) of the total land area (22.6 million ha) is salinized [5]. The same problem of soil salinity is observed in the southern part of the United States, the northern regions of China, and so on. Although the salts in low concentrations are not toxic to plants, when the concentration increases, they cause osmotic stress, preventing the flow of water entering the roots of plants. The consequence is physiological drought, leading to the death of the plants. In addition, at high concentrations of salts. ionic homeostasis is disrupted, which has a toxic effect and is a no less important cause of plant death.

Soil mapping is necessary to identify the centers of salinity and to plan the necessary agrotechnical measures.

Traditionally, to perform such mapping, remote sensing data of the Earth's surface of the optical range [6,7], hyperspectral [8], multispectral [9], and radar data [10–12] are used. These data are in various ways "connected" with the results of land-based studies of salinity. Due to the labor-intensive nature of expeditions and laboratory measurements, the volume of ground-based data is usually very limited [12–14], in rare cases reaching several hundred values [15]. Consequently, a system is needed that would link data from remote monitoring of the Earth's surface with a small set of actual values describing the state of the soil or vegetation. Similar systems have recently been built on the basis of artificial intelligence systems [14] using one or more machine learning models [16,17]. However, the results of such studies are negatively affected by several factors.

First, the resolution of publicly available satellite imagery does not allow for the detection of low-dimensional areas of salinity. Second, the variability in environmental conditions, irrigation, and weather leads to changes that may not be reflected in detail in the satellite data processing. However, low-cost multispectral data from UAVs can be used to assess heterogeneous soil properties such as water content and electrical conductivity [18]. Examples of research on the application of multispectral and hyperspectral data from UAVs are numerous. Some of them are discussed in the next section. In this article, the authors describe a method of operational mapping of local salinity on the basis of multispectral images obtained from the UAV. The study was conducted in the southern part of Kazakhstan. The main contribution of this study is as follows:

- A method for mapping the local salinity of agricultural fields with high resolution based on multispectral images obtained from UAVs is developed;
- In the course of development, the dataset was prepared, the possibility of applying machine learning algorithms of different types was investigated, the set of the model input parameters was optimized, and quantitative and qualitative comparison of the obtained results with the results of a similar model based on satellite data was performed.

The work consists of the following sections:

- The next section gives examples of the use of UAVs to assess the salinity of agricultural fields;
- Section 3 describes the methodological scheme of the study, including the processes of data collection and processing, machine learning models, method of optimization of the set of input parameters, etc.;
- Section 4 discusses the obtained results;
- In the Conclusion Section, the advantages and limitations of the proposed method are presented, and further research tasks are formulated.

2. Related Works

UAVs, as a relatively cheap and accurate tool, can be very useful in precision farming [19]. In recent years, the use of UAVs for the application of herbicides and fertilizers [20,21], as well as the mapping and classification of cultivated plants, weeds, and plant diseases [22–24], has been investigated. As a rule, such studies are based on machine learning methods [25]. One of the factors that reduce the efficiency of agriculture is the increased content of salts in the soil, which is commonly divided into five or six classes depending on the effect exerted on the growth of cultivated plants [26–28] (see Table 1).

Table 1. Threshold values of six classes of soil salinity and its effect on plant growth.

Salinity Class	$EC_{1:5}$ Range for Loams (dS/m)	Effect on Crop Growth	Types of Crops Growing at a Given Level of Salinity
Non-saline	0–0.18	Minor	All grains except corn, vetch, alfalfa
Slightly saline	0.19–0.36	Yields of salinity-sensitive crops may decrease	Cotton, timothy, hedgehog, melilot, wheat
Moderately saline	0.37–0.72	Yields of most crops decrease	rutabaga, fodder cabbage, wheatgrass, sorghum
Highly saline	0.73–1.45	Only salt-tolerant crops can give a satisfactory yield	sugar beets, sunflowers, western couch grass, French ryegrass, awnless bromegrass
Extremely saline	1.46–2.90	Only some of the most salt-tolerant crops can produce a satisfactory yield	
Extremely saline	>2.90		

Note. $EC_{1:5}$ is electrical conductivity of the soil solution (one weight fraction of soil dissolves in five fractions of water.

A quantitative analysis of soil salinity in the root zone is necessary to assess soil fertility and to develop measures for land reclamation and restoration. Such studies have been carried out for decades, based on relatively labor-intensive field studies and satellite data [3,14,29–31]. Nevertheless, the salinity factor remains difficult to identify quickly, changing in time and space [32]. UAVs are a valuable tool for operational monitoring of the Earth's surface. In this regard, there are studies aimed at recognition and assessment of salinity using UAV data.

The number of scientific works in this area shows a more than twofold increase from the end of 2020 (4730) to the beginning of 2023 (9760), which is a sign of a dynamically developing field of scientific research [33]. The UAV in these studies acts as a platform, equipped with cameras and sensors whose optimal combination is studied for different application conditions. For example, in the work [34], the UAV was equipped with a portable spectrometer with six spectral bands and was used to observe the dynamic change of soil salinity in the period before and after irrigation. The authors collected 120 soil samples and calculated 25 spectral covariates, from which the most salinity-sensitive ones were then selected using selection methods such as Variable Importance in Projection (VIP), competitive adaptive sampling with re-weighting (CARS), and the genetic algorithm (GA).

The combination of a genetic algorithm for feature selection and a feed-forward neural network (FFNN) for regression reconstruction showed the best result: the coefficient of determination R^2 was 0.78. The authors found that the higher the initial soil salinity was, the better the salinity reduction appeared after irrigation. Similarly, a UAV with a multispectral camera was used to estimate the degree of salinity in a highly saline area (Huanghekou City, Canli District) [35]. In this case, the support vector machines (SVM) model showed $R^2 = 0.835$.

The work [36] used a multispectral camera mounted on board a UAV to assess the quantitative content of salt in the soil. The authors conducted field studies (60 soil samples in the Shahaoku area in Inner Mongolia, China). The multispectral data were converted into 22 spectral covariates, from which the most sensitive ones were then selected. The authors compared three machine learning models random forest regressor (RFR), SVM, and FFNN. The best results of $R^2 = 0.835$ were obtained for the RFR model with VIP feature selection method.

A UAV equipped with a multispectral camera was used to estimate the volumetric water content in soil (VWC) and electrical conductivity (EC) [18]. The authors built a model based on RFR using a large number of ground-based measurements and found that the most useful were those multispectral data that penetrated deeper into the soil cover or were sensitive to bare soil.

The authors of [37] used multispectral imagery to estimate salt content changes in the irrigated sunflower fields (Hetao District, Inner Mongolia) during the growth stages of the plant. The FFNN-based model showed the best results. The authors positioned the obtained result as a fast and inexpensive method of salinity monitoring. In a similar paper [38], the authors aimed at effective prediction of soil salinity (electrical conductivity) using visible and near-infrared (Vis-NIR) spectroscopy. The authors proposed an optimal band combination algorithm OBCA and used RFR to estimate and map surface soil salinity using UAV.

In the work [39], UAV multispectral data, correlation analyses, and three machine learning algorithms were used to construct the soil salinity inversion models. The FFNN model had the highest inversion accuracy with $R^2 = 0.774$.

The work [40] is one of the first papers devoted to the application of a hyperspectral camera installed on board a UAV for field salinity assessment. The possibilities of similar application of UAVs for monitoring the soil cover of three types of agricultural fields differing in the amount of vegetation were investigated. The random forest regressor model linked field data and multispectral data.

Recently, a fairly common technique is the combination and comparison of images obtained from the UAV and satellite images [41,42]. The authors of [43] showed that the results of calculations of spectral indices of vegetation and soil properties obtained using UAVs and the Sentinel 2A are comparable. UAVs were more successful in assessing pH, sand, silt, and CaCO3 compared to the Sentinel 2A. Reference [44] proposes a monitoring method based on combining UAV multispectral remote sensing data, Sentinel-2A satellite remote sensing data, and ground-based salinity measurements in the Huanghe River Delta. The FFNN-based model showed $R^2 = 0.769$. Using this combined method, the authors found that the area of non-saline and weakly saline lands decreased, while the area of medium and highly saline soils and salt marshes increased. Moreover, this tendency was most strongly shown on unused lands and pastures.

In the assessment of the salinity in cultivated plans, there are no reference datasets based on which the applied methods can be compared. Not only do geographic and weather conditions differ, but the equipment that is available to researchers also differs. Therefore, a direct comparison with the results presented in the articles of various researchers is not entirely justified. For example, the study [44] in total uses more data (UAV multispectral remote sensing data, Sentinel-2A satellite remote sensing data). However, the result is somewhat worse than in [35,36], where only UAV-borne multispectral data are used.

Based on the literature review, it can be concluded that the use of a UAV as a low-altitude platform equipped with a multispectral or hyperspectral camera allows for performing the operational mapping of salinity in agricultural fields. However, the results are highly dependent on local conditions and the selected machine learning algorithms.

In this paper, we have in a sense continued the research described in the above listed papers, including the application of different types of machine learning algorithms and the comparison of results obtained from satellites and UAVs.

3. Method

The methodological scheme of the study consists of the following stages (Figure 1):

- Collection of soil samples and measurement of the electrical conductivity of the soil solution;
- Flight over the mapped area of the field with the help of a UAV equipped with a multispectral camera;
- Generation of field maps from overlapping images in different spectral ranges;
- Data pre-processing and calculation of spectral indices based on five spectral camera channels;
- Setting up a machine learning model;
- Salinity map calculation.

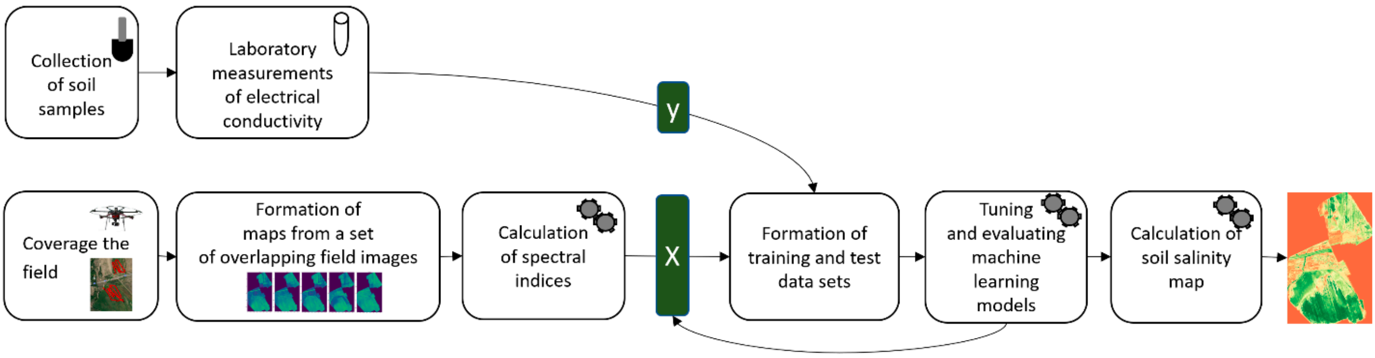

Figure 1. Scheme of research performance.

3.1. Preparation of the Dataset

The data source for training machine learning models was field studies, during which soil samples were collected and their geographic coordinates were recorded using a GPS device (Garmin 65) with a positioning accuracy of $\leq$5 m). The accuracy of the device is not high, which caused the need for further pre-processing of the data obtained from the UAV. A total of 80 soil samples were collected in one day (23 May 2022). Samples were collected at a distance of 20 m from each other in two adjacent fields. Figure 2 illustrates the location of the fields under the study, the appearance of one of the fields, and the processes of collecting soil samples.

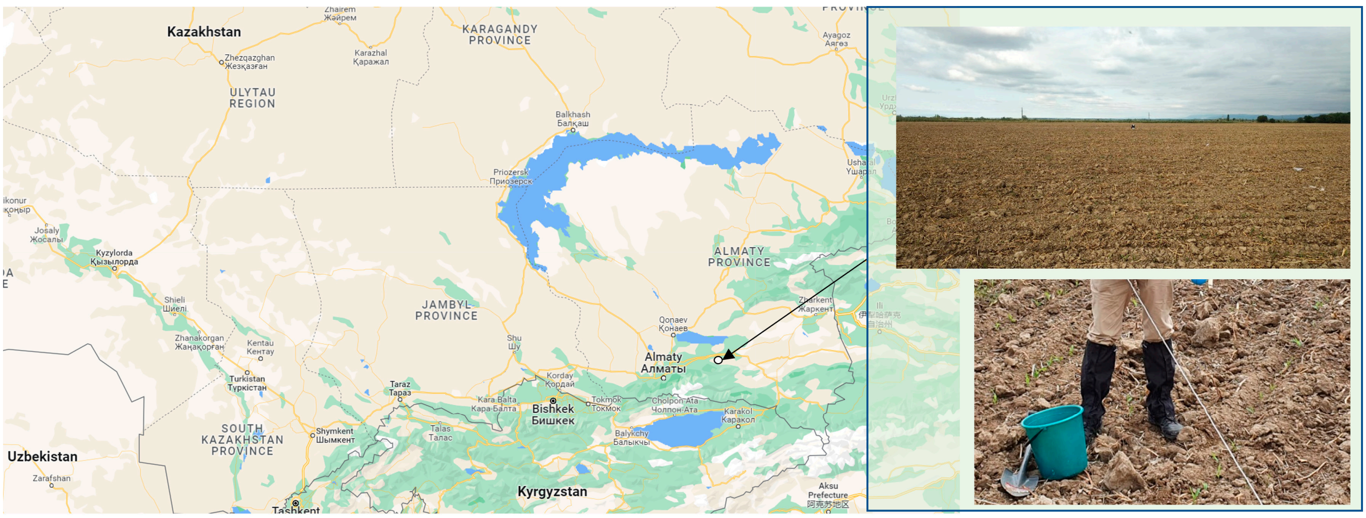

Figure 2. Location of the study field and the process of collecting soil samples.

On the same day, a specially designed hexacopter equipped with a MicaSense RedEdge-MX multispectral camera was used to fly over the field. Figure 3 shows the central part of the UAV with the installed camera and the path of the UAV movement. See Appendix A for a table of spectral ranges of the MicaSense RedEdge-MX camera. Note that the underlying surface in Figure 3b is not related to the date of the research. The real state of the vegetation at the time of the flight is shown in Figure 2. There are seedlings on the field, but the main signal was received from the bare soil surface.

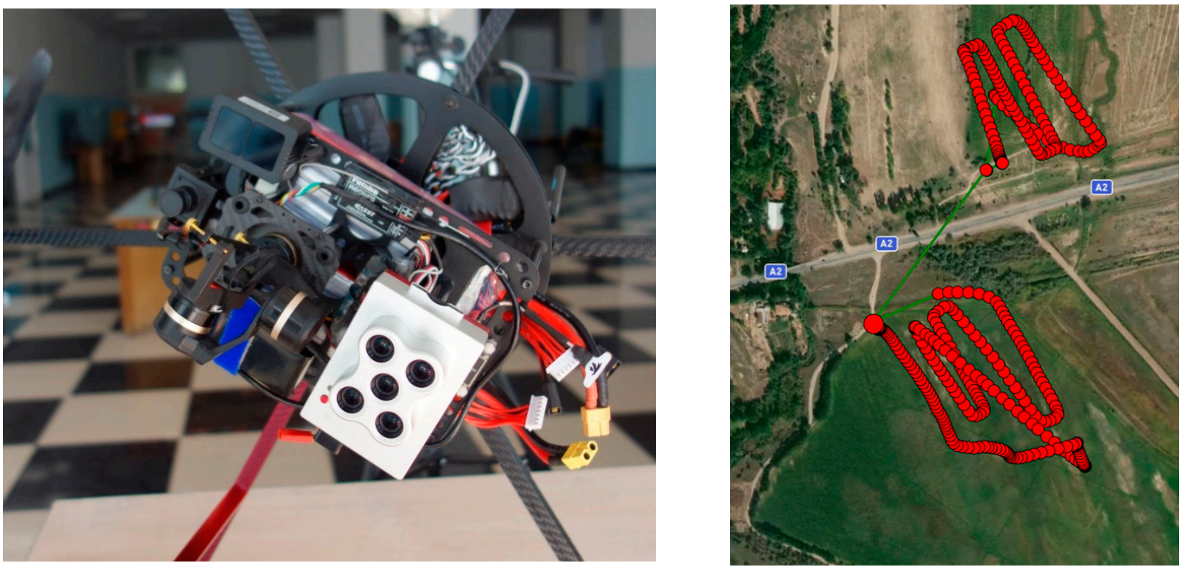

(**a**) (**b**)

Figure 3. Installation of a MicaSense RedEdge-MX camera (white camera) on a stabilized UAV suspension (**a**) and a field coverage map (**b**). Red dots show the UAV's flight path, A2—highway number.

The collected soil samples were dried, crushed, and sieved to remove solid insoluble fractions and vegetation residues. Then, they were mixed with water in a 1:5 ratio as is customary in many cases when measuring the electrical conductivity of a soil solution [12,14]. Figure 4 shows the stages of solution settling (a) and the calibration process of the Hanna GroLine HI9814 (b), which was used to measure conductivity. The prepared solutions were allowed to settle for at least one day in order to have time to dissolve the sparingly soluble fractions. Appendix B shows the coordinates of the soil samples and conductivity values.

(**a**) (**b**)

Figure 4. Preparation of soil solutions and instrument calibration before the measurements. The stages of solution settling (**a**) and the calibration process (**b**).

The electrical conductivity of the solution determines the 6 or lesser number of salinity classes according to Table 1 [28].

3.2. Data Pre-Processing

The obtained multispectral images of the field were combined into single maps using Pix4D [45] tools. Each spectral range corresponds to a separate map (Figure 5).

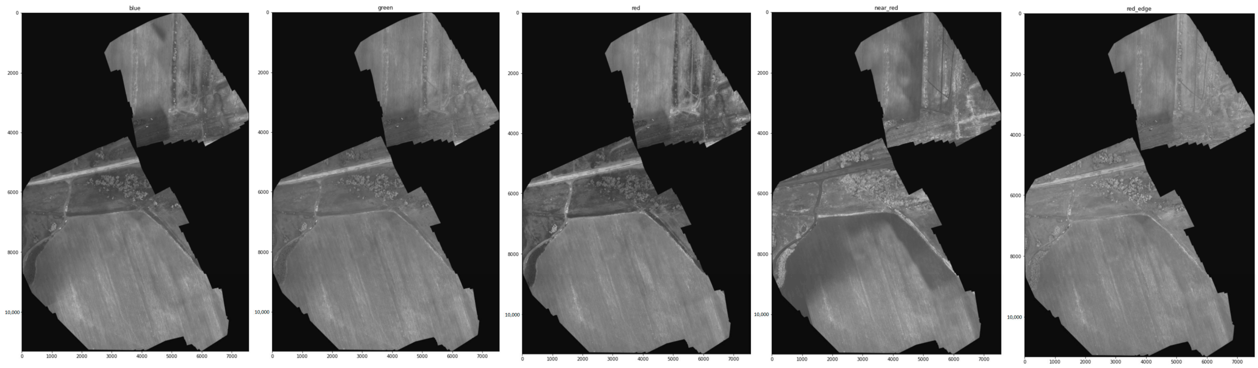

Figure 5. Images of the fields obtained in different spectral ranges. From left to right: blue, green, red, near_red, red_edge.

The resolution of images obtained from the UAV is about 7 cm. The ultra-high spatial resolution of UAV images may contain noise associated with the presence of shadows from small clumps of ground, depressions, and elevations. In addition, the accuracy of coordinate measurement on the surface is more than 1 m. The combination of these factors led to a significant (more than 20%) decrease in the quality of the salinity prediction based on machine learning. Similar difficulties were encountered by the authors of [40]. To improve the quality, several smoothing methods can be applied, for example, Gaussian Smoothing (GS):

$$G(x,y) = \frac{1}{2\pi\sigma^{2}} e^{-\frac{x^2+y^2}{2\sigma^2}}$$

where σ is the standard deviation of the distribution, and x, y are coordinates.

In our case, the method of averaging image pixel values in the range from 3 to 10 turned out to be useful for improving the prediction quality. In the course of computational experiments, the optimal size of the averaging filter was found, which was 5×5 pixels. In other words, we used average pooling with a filter size of 5×5 and a step of 1. Padding with size 2 was used to keep the size of original image. Figure 6 illustrates the process of applying average pooling to the original image. The pixels of padding are marked in white. Experiments have shown that the use of average pooling gives some improvement in the quality of the model compared to GS.

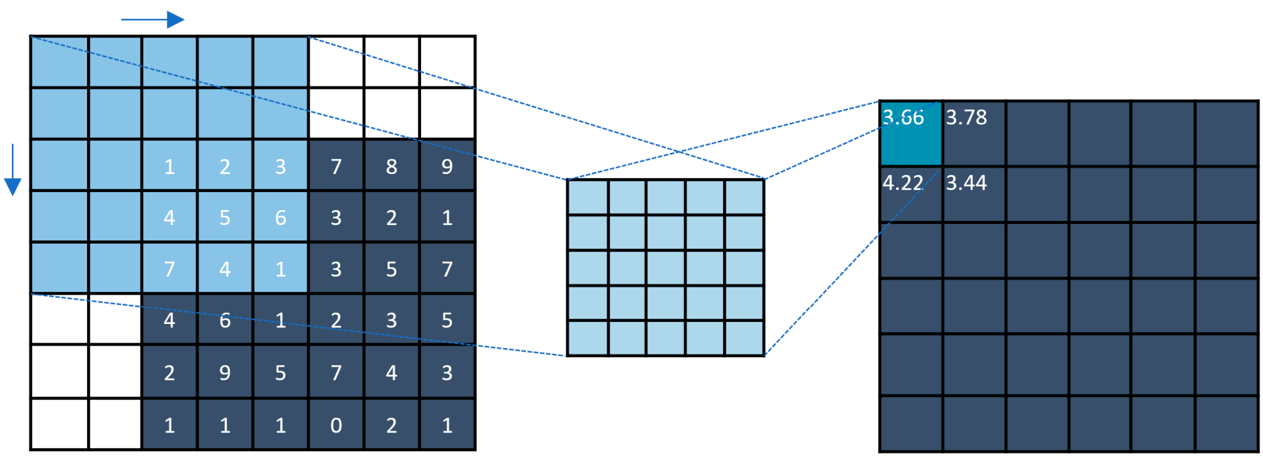

Figure 6. Applying a 5×5 average pooling filter to the original image (numbers are conditional).

The obtained data were used to calculate the spectral indices listed in Table 2. To use the "red_edge" range data, the additional spectral indices are proposed using this range instead of "nir" (marked with "*").

Table 2. Spectral indices used as input data for machine learning models.

Spectral Indices	Ref.
$NDSI = \frac{red - nir}{red + nir}$	[46]
$S1 = \frac{blue}{red}$	[47]
$S2 = \frac{blue - red}{blue + red}$	[47]
$S3 = \frac{green * red}{blue}$	[47]
$SI1 = \sqrt[2]{green * red}$	[48]
$SI2 = \sqrt[2]{green^2 + red^2 + nir^2}$	[49]
$SI3 = \sqrt[2]{green^2 + nir^2}$	[50]
$SI8 = \frac{blue * red}{green}$	[51]
$WI1 = 0.1761 * \text{green} + 0.322 * \text{red} + 0.3396 * \text{nir}$	[52]
$\text{SSRI} = \frac{nir}{\sqrt[2]{green * red}}$	[53]
$NDSIre = \frac{red - red\_edge}{red + red\_edge}$	*
$SI3re = \sqrt[2]{green^2 + red\_edge^2}$	*
$\text{SSRIre} = \frac{red\_edge}{\sqrt[2]{green * red}}$	*

Note. * Spectral index uses "red_edge" instead of "nir".

The calculated values of spectral indices for soil sample collection sites are presented in Appendix C.

3.3. Machine Learning Models

A wide range of machine learning algorithms, both classical and modern [15], can be used to build a regression model linking a set of input variables with the salinity value. Obviously, the application of deep learning models could give good results. However, their application requires a large set of initial data of the size of thousands and hundreds of thousands of lines. The available data are not sufficient. The authors are also not aware of large sets of labeled data obtained from the UAV or pre-trained models of deep neural networks solving the salinity estimation problem, which would allow for applying the transfer learning techniques [54] to tune it. For these reasons, the use of deep learning models is not reasonable. The authors conducted preliminary experiments with boosting models [55], support vector machines, and, as a reference point (base line) for comparative analysis, with classical regression algorithms (see Table 3).

Table 3. Machine learning models.

Regression Model	Abbreviation	References
XGBoost	XGB	[56]
LightGBM	LGBM	[57–59]
Random forest	RF	[60]
Support vector machines	SVM	[61]
Linear regression	LR	[62]
Lasso regression	Lasso	[63]
Ridge regression	Ridge	[64,65]
Elastic net	ElasticNet	[66]

To assess the quality of the regression models, accuracy indicators [67] are used, including the coefficient of determination (R^2), the mean square error (MSE), and the mean absolute error (MAE) (see Table 4).

Table 4. Quality metrics of regression models.

Accuracy Index	Abbreviation	Equation	Explanation
Determination coefficient	R^2	$R^2 = 1 - \frac{SS_{res}}{SS_{tot}}$ $SS_{res} = \sum_{i=1}^{m_k} \left(y^{(i)} - h^{(i)}\right)^2$ $SS_{tot} = \sum_{i=1}^{m_k} \left(y^{(i)} - \overline{y}\right)^2, \overline{y} = \frac{1}{m_k} \sum_{i=1}^{m_k} y^{(i)}$	where $y^{(i)}$ is the actual value; $h^{(i)}$ is the estimated value (hypothesis function value) for the *i-th* sample; and $m_k \in m$ is a part of the training sample (the set of marked objects).
Mean Absolute Error	MAE	$MAE = \frac{\sum_{i=1}^{n} \lvert y^{(i)} - h^{(i)} \rvert}{n}$	where n is simple size; when evaluating the performance of the model on the test set, n is the size of the test set.
Mean squared error	MSE	$MSE = \frac{\sum_{i=1}^{n} \left(y^{(i)} - h^{(i)}\right)^2}{n}$	

The MLextend library [68,69] was used to optimize the set of input parameters. To evaluate the models, the method of cross-validation of random permutations (ShuffleSplit) was used. In this case, the raw data are divided into the training and test samples randomly in a given proportion (in this case, 80% are training data, and 20% are test data). To ensure the statistical significance of the result, such splitting was performed 200 times for each regression model. The obtained values of the estimates were averaged, and the variance was calculated for them using the statistics library.

4. Results and Discussion

The results of the machine learning models are shown in Tables 5 and 6. Table 6 shows the results of models with the full set of input variables listed in Table 2. Using a large list of features with a small number of training examples can have a negative effect. Therefore, as in many similar research studies, we optimized the number of input variables of the model. Table 6 shows the results obtained with optimized set of features ('SI1', 'SI3', 'NDSI', 'SSRI', 'S1', 'S2', 'S3', 'NDSIre'). The optimization was performed using both the Sequential Backward Feature Selection (SBS) and Sequential Forward Selection (SFS) methods of mlextend library. The goal of the optimization was to find a combination of features that provides the maximum R^2 value.

Table 5. Results of machine learning models with the full set of input parameters.

Regressor	MAE	MSE	R^2	VarMAE	VarMSE	VarR^2	Duration
XGB	0.538	0.586	0.663	0.028	0.147	0.02	12.40934
RF	0.577	0.695	0.575	0.026	0.141	0.04	4.963758
LR	0.956	2.684	−0.749	0.094	13.405	6.872	0.112692
Lasso	1.131	1.864	−0.131	0.031	0.403	0.075	0.092753
ElasticNet	1.131	1.864	−0.131	0.031	0.403	0.075	0.08577
LGBM	0.738	1.03	0.384	0.031	0.236	0.037	2.12528
Ridge	0.795	1.141	0.328	0.034	0.302	0.034	0.16456
SVM	0.545	0.587	0.643	0.017	0.103	0.027	0.107743

Table 6. Results of machine learning models with an optimized set of input parameters.

Regressor	MAE	MSE	R^2	VarMAE	VarMSE	VarR^2	Duration
XGB	0.514	0.508	0.701 *	0.014	0.051	0.012	65.93539
RF	0.562	0.641	0.597	0.02	0.09	0.037	11.2957
LR	0.808	1.171	0.233	0.03	0.299	0.202	0.165049
Lasso	1.112	1.782	−0.099	0.029	0.317	0.036	0.159441
ElasticNet	1.112	1.782	−0.099	0.029	0.317	0.036	0.164228
LGBM	0.716	0.947	0.421	0.026	0.15	0.024	3.062773
Ridge	0.841	1.2	0.272	0.029	0.237	0.028	0.346673
SVM	0.547	0.604	0.623	0.017	0.078	0.025	0.220766

N.B. varMAE, varMSE, VarR^2 are the variances of the obtained estimates, and Duration is the model training time in seconds (Intel Core i7-10750H, 2.60 GhZ, 32Gb). * The maximum value of R^2 is 0.67 when using GS with parameter σ = 25.

The results show that the application of the optimized set of features led to a significant improvement in the quality of the XGB model. Relatively good results can also be obtained using RF and SVM. This indicates the robustness of the method to changes in the machine learning model. Salinity mapping results using XGB are shown in Figure 7.

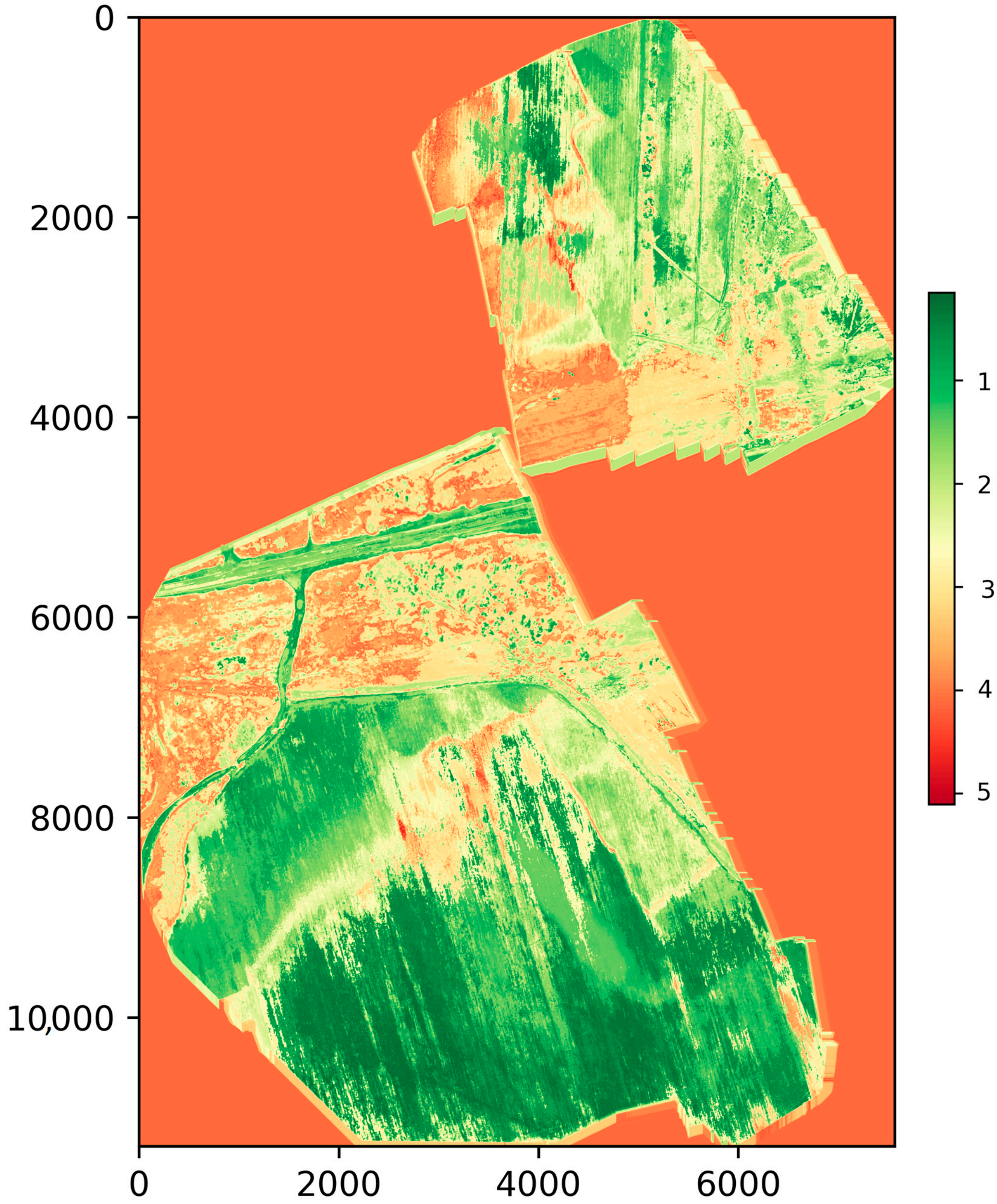

Figure 7. Salinity levels of the study field areas.

Figure 8 shows the salinity of the soil cover of the field in black and white. The areas with increased salinity are highlighted in white. The colored dots show the places where soil samples were collected. The color of the dot in the figure determines the value of the measured salinity according to Table 1, so that blue indicates non-saline, green indicates slightly saline, yellow indicated moderately saline, red indicates highly saline, and crimson indicates severely saline and extremely saline for loamy soils.

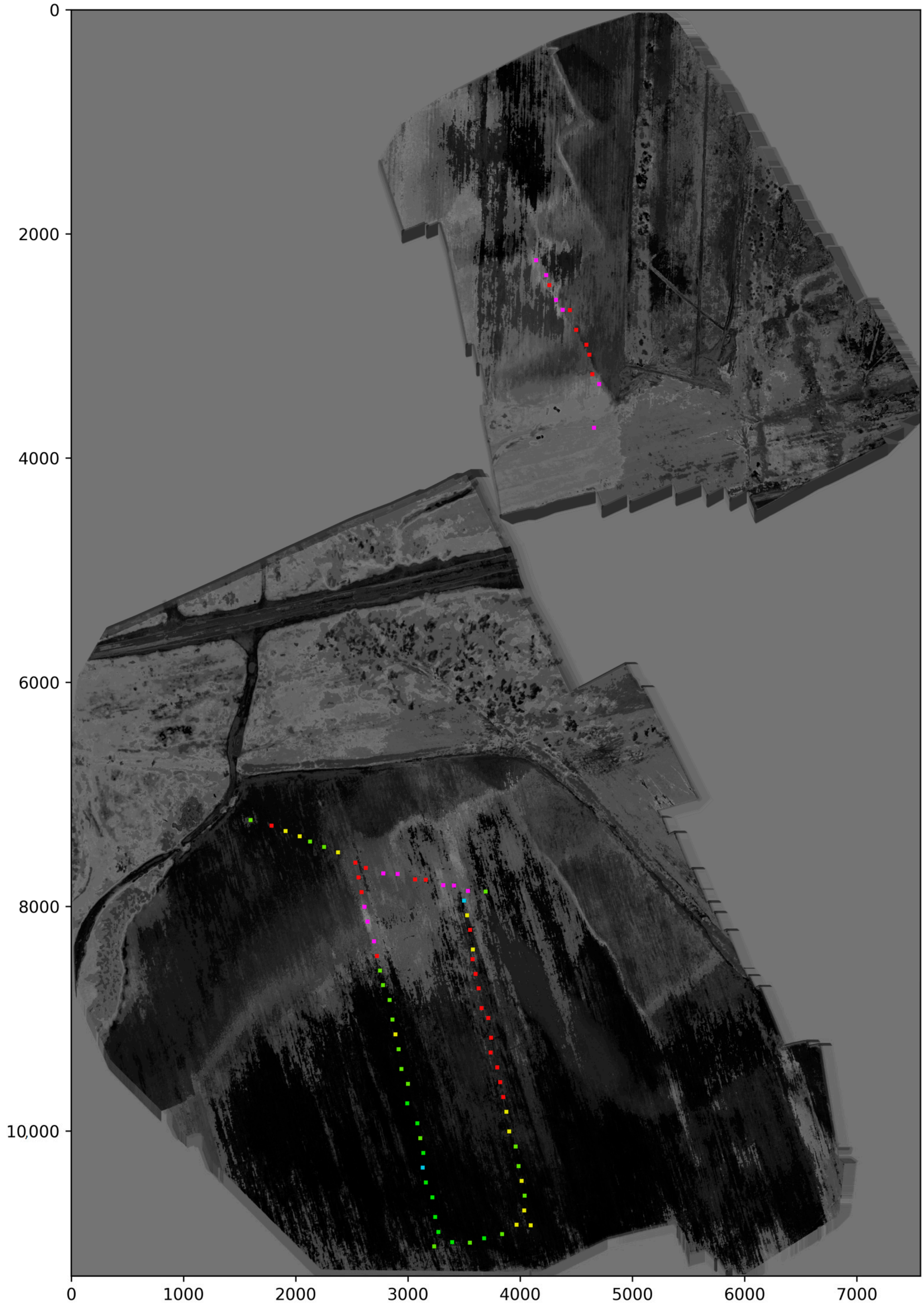

Figure 8. Salinity of the field (light areas are saline areas, dark areas are not saline areas). Colored dots indicate sample collection sites.

It can be seen that the values of salinity of soil samples agree well with the received map of salinity. The map as a whole allows for presenting the processes on the fields with a high degree of detail.

To compare the quality of field mapping, similar studies were performed using Landsat 8 optical data. Figure 9 shows a section of the land surface mapped by the XGB model using optical satellite data from 2 April 2022. On the right side of Figure 9 is the map shown above (Figure 7) at the appropriate scale. The coefficient of determination of the XGB regressor from the satellite data was 0.54. The resolution of the satellite image is 30 m, while the resolution of the UAV image is about 7 cm. For this reason, the details of local salinity in the studied fields are difficult to discern when using satellite data.

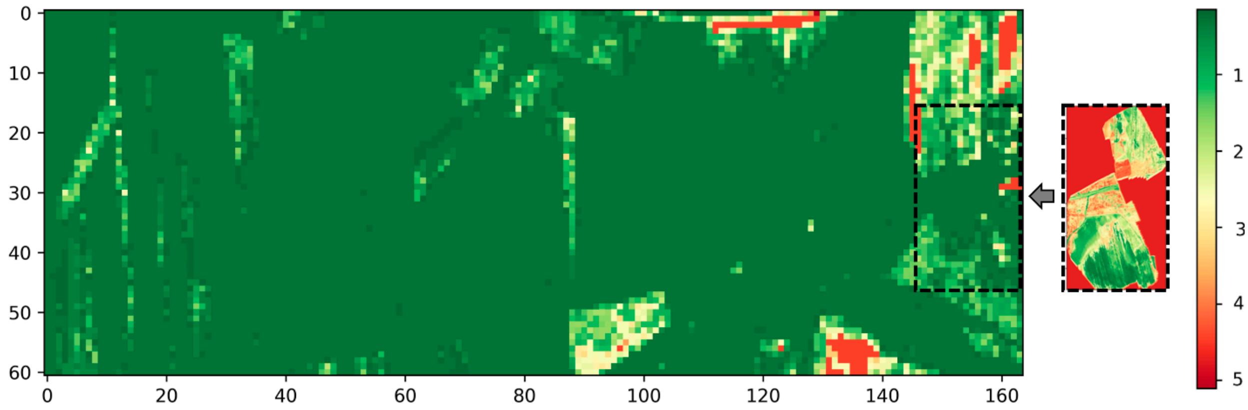

Figure 9. Map of salinity of agricultural fields in the Shelek area based on the satellite data.

The result of salinity studies may depend on both the type of soil and the geographical conditions for the formation of salt deposits. The reliability of the proposed method is based on the following assumptions:

(1) The entire region under consideration is located on the sloping foothill plain of the Zailiysky Alatau ridge, formed by the alluvial fans of the river system. This somewhat evens out the soil differences. Soil waters are formed by surface/underground runoff from a mountain range are initially fresh. Salinization is confined to small salt lenses that exist in the upper part of the sedimentary cover and the lower parts of small river basins. One of the peculiarities of salinization of the region is the fixedness of places of pronounced salinity, the level of which varies every year depending on the water content of the year (less in high water, more in low water). Therefore, the characteristic relationship between the soil types and their salinity in this region is not expressed as clearly as in the plains with saline groundwater (for example, the oases of Central Asia).

(2) The spectral characteristics depend on the composition of the soil. The color factor of mineral components and the content of humus influence affects it. However, fields are organized only in places with a developed layer of fertile soil in which mineral components and humus do not have significant variations.

5. Conclusions

The performed study leads to the conclusion that mapping the salinity of cultivated fields using UAVs can be more accurate and more detailed than using publicly available satellite images. The sufficiently high accuracy, the possibility of using UAVs on cloudy days, and the high speed of obtaining maps make such a method of mapping very attractive. Essentially, the map can be obtained within 1 day if the technological processes of soil sample processing are not taken into account.

However, it should be noted that this method, as well as other methods of this kind, has limitations:

1. Dependence on weather conditions, field humidity, illumination, presence of plants, etc.;

2. UAV use is limited by weather conditions. Rain and strong winds make overflights ineffective or impossible.

In addition, this particular study also has limitations:

3. A small number of ground measurements in one single day;
4. One kind of soil with little vegetation. However, for example, Reference [70] indicates that salinity estimation models may be different for bare ground and vegetated areas.

Based on the existing limitations of the current study, we plan the following for the future:

5. Additional verification of the method is required depending on the changes in weather conditions, soil moisture, presence of plants, etc.;
6. It is necessary to expand the area of field studies of fields and soils essentially different from those mentioned in this work. In particular, it is useful to carry out the analysis on sandy soils, which are very typical for the southern regions of Kazakhstan;
7. In general, despite the noted limitations, the described method of mapping of salinity of cultivated fields is quite accurate, operational and low-cost. Its wide application in the practice of precision farming requires relatively little effort to develop specialized software and unmanned flying platforms.

Author Contributions: Conceptualization, R.M. and Y.K.; methodology, R.M. and A.T.; software, R.M. and Y.K.; validation, A.T., E.Z. and V.L.; investigation, R.M., L.T., A.T. and A.S.; resources, R.M., Y.K. and M.Y.; data curation, Y.K., A.T., M.A. and L.T.; writing—original draft preparation, R.M., T.M., and Y.K.; writing—review and editing, Y.P., M.Y. and A.S.; visualization, R.M., Y.K. and M.A.; supervision, R.M.; project administration, Y.A.; funding acquisition, Y.A., E.Z. and V.L. All authors have read and agreed to the published version of the manuscript.

Funding: This research was funded by the Committee of Science of the Ministry of Science and Higher Education of the Republic of Kazakhstan, under Grants: AP14869972 "Development and Adaptation of Computer Vision and Machine Learning Methods for Solving Precision Agriculture Problems Using Unmanned Aerial Systems"; Grant BR10965172 «Space monitoring and GIS for quantitative assessment of soil salinity and degradation of agricultural lands in South Kazakhstan»; BR18574144 «Development of a Data Mining System for Monitoring Dams and Other Engineering Structures under the Conditions of Man-Made and Natural Impacts"; and AP09259597 "Develop and implement methods for managing the sugar beet production process for technologies of various levels of intensification in the precision farming system". This work was partially supported by the Slovak Research and Development Agency, Slovakia under grant "New methods development for reliability analysis of complex system" (APVV-18–0027) ".

Data Availability Statement: The data presented in this study are openly available in https://www.dropbox.com/sh/9rlcdbb6fcbawwq/AABMc_TTniUAaoUftleFob8wa?dl=0.

Conflicts of Interest: The authors declare no conflict of interest.

Appendix A

Table A1. Table of spectral ranges of the multispectral camera MicaSense RedEdge-MX [71].

File Suffix	Band Name	Center Wavelength (nm)	Bandwidth (nm)
1	Blue	475	32
2	Green	560	27
3	Red	668	14
4	Red Edge	717	12
5	Near IR	842	57

Notes: (1) The Band Name tag contains the human-readable name (Blue, Green, etc.); (2) The Central Wavelength tag contains the center wavelength of the filter for that band in nanometers (475, 560, etc.); (3) The Wavelength FWHM tag contains the bandwidth of the filter (32, 27, etc.).

Appendix B

Table A2. Results of laboratory testing of soil samples.

Sample Number	X	Y	Elco50
1.	265,440.44	4,828,020.66	0.37
2.	265,453.74	4,828,017.08	1.59
3.	265,462.59	4,828,013.66	0.74
4.	265,471.53	4,828,010.34	0.82
5.	265,478.13	4,828,007.00	0.58
6.	265,486.98	4,828,003.57	0.51
7.	265,495.84	4,828,000.15	0.77
8.	265,506.85	4,827,993.65	2.6
9.	265,513.44	4,827,990.30	2.33
10.	265,524.56	4,827,986.80	2.92
11.	265,533.53	4,827,986.49	3.24
12.	265,544.64	4,827,982.99	2.45
13.	265,551.43	4,827,982.75	2.51
14.	265,562.47	4,827,979.36	4.11
15.	265,569.25	4,827,979.12	3.28
16.	265,578.11	4,827,975.70	2.97
17.	265,589.33	4,827,975.31	0.43
18.	265,657.99	4,828,269.49	3.23
19.	265,661.22	4,828,297.17	4.68
20.	265,656.91	4,828,303.44	2.1
21.	265,655.08	4,828,315.85	1.78
22.	265,653.12	4,828,322.14	1.54
23.	265,646.66	4,828,331.60	2.16
24.	265,642.65	4,828,344.08	2.68
25.	265,638.12	4,828,344.24	4.65
26.	265,633.90	4,828,350.62	4.22
27.	265,629.70	4,828,359.99	2.86
28.	265,627.66	4,828,366.29	4.27
29.	265,621.27	4,828,375.74	5.11
30.	265,575.63	4,827,969.56	0.15
31.	265,577.57	4,827,960.26	0.82
32.	265,579.51	4,827,950.97	2.23
33.	265,581.25	4,827,938.56	1.15
34.	265,581.04	4,827,932.34	1.95
35.	265,582.98	4,827,923.04	1.67
36.	265,584.91	4,827,913.63	1.94
37.	265,586.74	4,827,901.23	1.61
38.	265,590.97	4,827,894.96	1.68
39.	265,592.80	4,827,882.56	2.17
40.	265,592.47	4,827,873.23	1.73
41.	265,596.68	4,827,863.85	1.48
42.	265,598.53	4,827,854.55	2.4
43.	265,600.47	4,827,845.15	1.65
44.	265,602.41	4,827,835.85	0.78
45.	265,604.24	4,827,823.44	1.09
46.	265,608.35	4,827,813.96	0.65
47.	265,610.18	4,827,801.55	0.54
48.	265,612.12	4,827,792.25	0.8
49.	265,614.06	4,827,782.95	0.41
50.	265,613.74	4,827,773.62	0.8
51.	265,617.86	4,827,764.25	0.95
52.	265,608.89	4,827,764.56	1.11
53.	265,599.71	4,827,758.66	0.66
54.	265,588.38	4,827,756.05	0.3
55.	265,579.31	4,827,753.25	0.39

Table A2. *Cont.*

Sample Number	X	Y	Elco50
56.	265,568.08	4,827,753.65	0.33
57.	265,556.75	4,827,750.93	0.52
58.	265,559.33	4,827,760.07	0.24
59.	265,557.39	4,827,769.48	0.22
60.	265,555.56	4,827,781.88	0.21
61.	265,551.44	4,827,791.26	0.22
62.	265,549.51	4,827,800.67	0.18
63.	265,549.83	4,827,809.89	0.25
64.	265,547.89	4,827,819.18	0.41
65.	265,546.04	4,827,828.59	0.34
66.	265,539.68	4,827,841.15	0.32
67.	265,540.12	4,827,853.48	0.52
68.	265,536.00	4,827,862.86	0.5
69.	265,534.17	4,827,875.26	0.47
70.	265,532.23	4,827,884.67	0.73
71.	265,530.29	4,827,893.97	0.47
72.	265,528.54	4,827,906.37	0.51
73.	265,524.34	4,827,915.75	0.44
74.	265,522.41	4,827,925.16	0.53
75.	265,520.47	4,827,934.46	2.64
76.	265,518.61	4,827,943.75	4.08
77.	265,514.52	4,827,956.24	4.78
78.	265,512.58	4,827,965.65	3.82
79.	265,510.72	4,827,974.94	2.14
80.	265,508.79	4,827,984.24	2.23

Note. X,Y—UTM Coordinates (WGS 84/UTM zone 44N), elco50—electrical conductivity of soil solution (mS/cm) in a 1:5 ratio (1weight fraction of soil, 5 fractions of water).

Appendix C

Table A3. Results of laboratory testing of soil samples.

No.	X	Y	SI1	SI2	SI3	SI8	WI1	NDSI	SSRI	S1	S2	S3	NDSIre	SI3re	SSRIre
1	1581	7212	31,619.53	50,272.68	38,265.54	26,855.87	23,672.41	0.18	0.72	0.77	−0.13	39,585.04	−0.03	46,161.49	1.09
2	1768	7262	36,902.67	57,748.47	42,849.27	33,159.49	26,970.29	0.23	0.66	0.78	−0.12	45,200.5	−0.02	53,732.99	1.1
3	1893	7310	32,921.36	51,333.71	38,178.53	29,576.39	23,895.56	0.23	0.65	0.79	−0.12	39,813.86	−0.02	47,608.32	1.08
4	2019	7357	33,010.39	51,349.65	38,085.48	29,752.05	23,862.3	0.24	0.64	0.79	−0.12	39,872.31	−0.02	47,618.25	1.08
5	2111	7404	30,719.88	48,504.08	36,171.15	27,892.53	22,796.44	0.2	0.69	0.78	−0.12	37,439.93	−0.03	45,022.79	1.12
6	2236	7452	33,226.79	52,053.5	38,450.84	31,387.22	24,344.2	0.23	0.67	0.8	−0.11	39,222.96	−0.01	47,736.48	1.08
7	2360	7500	35,348.55	56,073.35	41,414.79	34,960.26	26,467.1	0.2	0.71	0.81	−0.11	40,876.01	0	50,395.36	1.08
8	2515	7592	35,662.25	58,124.9	44,140.12	36,537.35	27,808.53	0.14	0.8	0.86	−0.08	39,142.25	0	50,696.74	1.06
9	2608	7639	33,049.84	55,088.7	42,765.54	34,290.42	26,560.38	0.09	0.88	0.89	−0.06	35,166.48	0	46,729.64	1.05
10	2764	7688	31,692.16	54,250.04	42,231.75	34,138.8	26,423.22	0.06	0.95	0.87	−0.07	33,965.65	−0.01	45,455.36	1.09
11	2891	7693	31,623.7	54,135.65	42,211.09	34,733.63	26,361.6	0.06	0.95	0.89	−0.06	33,077.24	0	45,108.26	1.08
12	3047	7742	33,836.17	57,455.19	44,864.34	36,660.98	27,888.77	0.06	0.93	0.91	−0.05	35,140.63	−0.01	48,582.3	1.08
13	3142	7745	33,180.1	56,154.1	44,101.52	37,121.19	27,192.78	0.06	0.92	0.97	−0.01	32,551.17	−0.02	47,851.68	1.08
14	3298	7793	28,302.42	51,951.66	42,764.85	32,243.49	25,499.74	−0.06	1.17	1.01	0	26,986.63	−0.06	43,143.48	1.18
15	3393	7796	31,830.62	58,171.2	47,941.44	36,816.9	28,514.52	−0.05	1.16	1.04	0.02	29,483.93	−0.07	48,670.95	1.19
16	3518	7844	28,809.65	50,953	41,329	32,690.37	24,870.42	−0.01	1.06	1.03	0.01	27,167.72	−0.05	43,056.26	1.14
17	3676	7850	36,652.02	62,353.43	50,182.58	39,482.78	30,076.59	0.03	0.95	1.05	0.02	34,690.05	−0.01	52,410.36	1.03
18	4641	3712	17,135.32	36,037.67	31,811.91	12,363.02	17,563.23	−0.22	1.56	0.75	−0.14	23,191.42	−0.18	30,048.8	1.43
19	4687	3322	18,866.38	33,220.33	26,361.13	17,574.29	16,272.7	0.01	1.04	0.76	−0.14	23,254.51	−0.02	27,285.59	1.1
20	4626	3234	22,691.57	38,676.51	29,564	22,500.47	18,851.16	0.08	0.93	0.75	−0.14	27,636.87	−0.01	32,624.08	1.11
21	4600	3060	33,203.87	52,824.18	37,969.63	37,625.6	25,006.89	0.22	0.7	0.84	−0.09	35,845.31	0.05	44,901.57	1.01
22	4573	2971	32,427.78	51,010.03	36,666.08	38,304.16	23,965.03	0.24	0.67	0.9	−0.05	32,832.52	0.04	44,053.07	1
23	4482	2838	32,921.44	52,187.91	37,989.29	40,089.89	24,642.72	0.22	0.7	0.95	−0.03	31,938.03	0.03	45,087.98	1.01
24	4426	2662	40,692.84	63,848.23	46,228.53	48,593.76	29,935.59	0.24	0.66	0.94	−0.03	39,912.92	0.02	56,583.71	1.04
25	4362	2660	38,942.71	62,143.67	46,148.39	45,250.8	29,435.07	0.19	0.73	0.95	−0.02	38,279.15	0.03	53,260.41	1
26	4302	2571	39,133.77	63,776.54	48,770.95	44,064.17	30,479.83	0.13	0.8	0.97	−0.01	38,326.87	0.04	52,993.42	0.96
27	4243	2439	34,790.93	57,240.31	44,413.74	36,988.37	27,424.92	0.11	0.84	0.95	−0.03	35,250.87	0.01	48,600.75	1.01
28	4215	2350	35,444.48	59,136.38	46,432.02	37,978.31	28,459.76	0.08	0.88	0.97	−0.01	35,314.34	0	50,214.56	1.03
29	4125	2217	35,451.08	58,261.78	45,127.83	38,670.38	27,907.62	0.11	0.83	0.97	−0.01	35,115.12	0.03	48,569.08	0.98
30	3483	7931	34,922.95	62,428.28	50,977.04	39,099.33	30,509.75	−0.03	1.09	1.02	0.01	33,213.64	−0.05	52,285.2	1.14

Table A3. *Cont.*

No.	X	Y	SI1	SI2	SI3	SI8	WI1	NDSI	SSRI	S1	S2	S3	NDSIre	SI3re	SSRIre
31	3510	8062	34,775.61	62,081.32	50,418.22	39,061.78	30,373.29	−0.02	1.09	0.99	0	33,590.23	−0.04	51,539.51	1.13
32	3537	8192	36,464.78	65,414.32	53,606.98	40,862.6	31,967.33	−0.03	1.1	1.03	0.02	34,391.46	−0.05	54,472.73	1.13
33	3562	8367	35,937.93	65,005.76	53,847.66	40,009.17	31,731.84	−0.05	1.13	1.07	0.03	33,146.86	−0.06	54,514.4	1.15
34	3559	8454	32,990.46	60,012.68	49,807.56	36,945.76	29,319.25	−0.06	1.14	1.07	0.03	30,334.44	−0.07	50,175.57	1.16
35	3586	8585	35,196.92	65,087.31	54,362.26	39,155.04	31,856.38	−0.08	1.19	1.06	0.03	32,718.71	−0.07	53,919.28	1.17
36	3613	8717	33,364.48	62,219.95	52,621.7	35,825.76	30,368.09	−0.1	1.22	1.09	0.04	30,767.77	−0.08	51,519.84	1.17
37	3639	8892	32,155.03	59,371.89	50,182.94	33,485.06	28,915.25	−0.09	1.19	1.08	0.04	30,063.99	−0.07	48,993.18	1.14
38	3699	8980	33,462.17	62,456.36	52,956.81	35,364.47	30,456.96	−0.1	1.22	1.09	0.04	31,002.1	−0.08	51,433.51	1.16
39	3724	9155	35,861.23	64,369.39	53,239.48	38,386.89	31,369.61	−0.05	1.11	1.04	0.02	34,099.58	−0.04	52,841.87	1.09
40	3720	9286	34,615.44	62,465.31	51,272.79	37,694.58	30,560.08	−0.04	1.12	0.99	0	33,771.88	−0.01	49,719.5	1.06
41	3779	9418	35,286.84	63,214.13	51,761.6	37,214.93	30,887.77	−0.03	1.1	0.97	−0.02	35,382.62	−0.01	50,249.41	1.04
42	3805	9549	34,568.82	62,491.73	52,043.17	35,215.85	30,441.52	−0.06	1.13	1.02	0.01	33,982.58	−0.01	49,512.87	1.03
43	3832	9681	35,040.66	63,653.7	53,345.37	34,851.16	30,974.45	−0.07	1.14	1.02	0.01	34,606.16	−0.01	50,232.72	1.02
44	3860	9812	34,782.09	63,253.85	53,167.36	34,752.69	30,751.78	−0.07	1.14	1.04	0.02	33,789.66	−0.01	49,770.21	1.01
45	3885	9986	38,120.35	69,017.37	57,868.49	36,992.55	33,545.25	−0.07	1.13	1.01	0.01	38,241.08	−0.01	54,450.09	1.01
46	3943	10,120	38,509.9	69,106.52	58,017.35	37,339.58	33,476.99	−0.06	1.1	1.05	0.02	37,753.44	−0.01	54,989.23	0.99
47	3969	10,294	35,800.91	63,791.15	53,538.07	33,858.06	30,831.76	−0.06	1.08	1.04	0.02	35,530.28	−0.01	50,946.17	0.98
48	3996	10,425	35,597.9	63,462.99	53,268.57	33,265.45	30,677.29	−0.06	1.08	1.03	0.01	35,773.19	0	50,621.33	0.98
49	4023	10,556	38,549.36	67,230.32	56,317.83	35,299.47	32,249.99	−0.03	1.02	1.06	0.03	38,193.69	0	54,576.98	0.95
50	4019	10,687	34,644.84	61,485.42	51,746.9	31,698.76	29,633.54	−0.05	1.07	1.04	0.02	34,787.35	0	49,270.19	0.97
51	4077	10,819	38,040.29	65,878.63	55,051.47	34,430.74	31,542.16	−0.02	0.99	1.05	0.03	38,027.89	0	53,699.07	0.94
52	3951	10,814	34,619.85	61,563.29	51,782.52	31,708.75	29,701.74	−0.06	1.08	1.03	0.01	34,962.26	0	49,198.57	0.97
53	3822	10,897	39,478.28	70,041.44	58,892.43	36,511.13	33,769.16	−0.05	1.07	1.04	0.02	39,371.13	0	56,084.38	0.97
54	3662	10,934	39,081.14	68,990.71	57,838.46	36,107.53	33,247.39	−0.05	1.05	1.04	0.02	39,172.71	−0.01	55,624.08	0.97
55	3535	10,973	40,419.78	71,198.95	59,803.04	37,001.03	34,249.42	−0.05	1.05	1.05	0.02	40,347.18	−0.01	57,815.36	0.98
56	3377	10,968	35,463.97	61,632.84	51,616.5	32,955.44	29,522.39	−0.03	1	1.08	0.04	34,420.53	0	50,266.59	0.95
57	3217	11,006	36,481.61	64,096.52	54,003.98	33,718.02	30,749.1	−0.05	1.04	1.09	0.04	35,350.05	−0.01	52,069.96	0.96
58	3254	10,878	35,799.66	62,853.58	52,727.18	33,399.75	30,213.9	−0.04	1.04	1.07	0.03	35,042.66	0	50,885.24	0.96
59	3226	10,745	37,759.88	65,464.93	54,838.59	34,849.58	31,319.19	−0.03	1	1.09	0.04	36,682.98	0	53,337.31	0.94
60	3201	10,571	40,116.97	70,115.71	58,824.09	37,563.27	33,638.85	−0.04	1.02	1.09	0.04	38,759.64	0	56,880.92	0.95
61	3143	10,439	37,017.86	65,115	54,618.94	35,625.86	31,326.68	−0.04	1.04	1.1	0.05	35,275.89	0	52,314.1	0.95
62	3115	10,307	38,557.66	67,637.52	56,604.5	37,226.06	32,541.46	−0.04	1.03	1.09	0.04	36,822.72	0.01	54,252.12	0.95
63	3120	10,177	39,821.81	70,591.36	59,015.55	38,778.07	34,116.75	−0.05	1.07	1.06	0.03	38,689.51	0	56,617.9	0.98
64	3093	10,046	39,456.76	70,135.38	58,423.89	38,395.82	33,982.11	−0.05	1.08	1.02	0.01	39,213.12	0	55,857.15	0.98
65	3067	9914	38,455.8	68,614.93	57,187.06	38,477.1	33,280.44	−0.05	1.09	1.04	0.02	37,363.75	−0.01	54,696.65	1
66	2977	9737	41,507.14	74,130.67	61,961.22	41,722.18	35,923.95	−0.05	1.09	1.07	0.03	39,695.05	−0.01	59,209.85	1
67	2983	9564	43,112.79	76,763.88	63,652.19	44,378.2	37,283.02	−0.04	1.08	1.04	0.02	41,486.4	0	61,252.62	1
68	2925	9432	39,722.92	72,508.87	60,892.84	40,011.76	35,301.2	−0.08	1.15	1.04	0.02	38,728.58	−0.03	57,807.88	1.05
69	2900	9257	40,703.27	72,467.76	59,899.03	42,870.42	35,236.98	−0.04	1.08	1.05	0.02	38,807.26	−0.01	58,146.09	1.02
70	2872	9125	36,047.26	64,656.78	53,378.15	38,254.48	31,522.96	−0.04	1.1	1.02	0.01	34,800.43	−0.02	51,999.33	1.05
71	2845	8994	40,354.28	70,899.66	58,008.27	43,454.24	34,445.19	−0.02	1.04	1.04	0.02	38,242.59	−0.01	57,951.21	1.04
72	2820	8820	40,181.84	68,540.23	55,148.86	43,967.28	33,100.71	0.03	0.95	1.05	0.03	37,672.72	−0.01	57,608.12	1.04
73	2761	8688	37,574.88	62,579.63	49,616.42	41,335.21	30,017.73	0.07	0.88	1.05	0.03	35,186.03	−0.02	54,185.48	1.05
74	2734	8555	37,664.32	61,185.91	47,313.63	41,928.11	29,128.25	0.13	0.8	1.02	0.01	35,898.03	−0.02	54,462.54	1.07
75	2707	8425	38,269.51	61,302.54	46,459.25	42,898.79	29,036.6	0.17	0.75	0.98	−0.01	37,286.34	−0.02	55,150.67	1.08
76	2681	8294	37,392.37	60,150.85	45,227.45	42,530.39	28,597.92	0.17	0.76	0.95	−0.02	36,975.98	−0.01	53,642.44	1.08
77	2623	8118	29,107.63	47,998.65	37,013.66	32,611.44	23,050.11	0.11	0.84	0.97	−0.02	28,635.93	−0.02	42,260.48	1.1
78	2596	7986	30,821.13	49,796.85	38,004.57	33,595.66	23,687.6	0.15	0.78	0.96	−0.02	30,818.83	−0.01	44,070.66	1.06
79	2570	7855	31,888.41	52,176.3	40,028.92	33,969.96	24,977.03	0.12	0.82	0.92	−0.04	32,971.84	0	45,374.85	1.06
80	2543	7724	35,226.8	57,560.92	44,143.08	36,437.63	27,536.38	0.13	0.81	0.9	−0.05	37,451.61	0	49,713.54	1.04

Note. X,Y—coordinates of sample collection points in pixels.

References

1. Hossain, M.S. Present Scenario of Global Salt Affected Soils, Its Management and Importance of Salinity Research. *Int. Res. J. Biol. Sci.* **2019**, *1*, 1–3.
2. Qadir, M.; Quillérou, E.; Nangia, V.; Murtaza, G.; Singh, M.; Thomas, R.J.; Drechsel, P.; Noble, A.D. Economics of Salt-Induced Land Degradation and Restoration. *Nat. Resour. Forum* **2014**, *38*, 282–295. [CrossRef]
3. Li, X.; Wang, Z.; Song, K.; Zhang, B.; Liu, D.; Guo, Z. Assessment for Salinized Wasteland Expansion and Land Use Change Using GIS and Remote Sensing in the West Part of Northeast China. *Environ. Monit. Assess.* **2007**, *131*, 421–437. [CrossRef] [PubMed]
4. Toderich, K.; Khuzhanazarov, T.; Ibrayeva, M.; Toreshov, P.; Bozaeva, J.; Konyushkova, M.; Krenke, A. Innovative Approaches and Technologies to Manage Salinization of Marginal Lands in Central Asia 2022. Textbook. Nur-Sultan, FAO (In Russian). Available online: https://www.fao.org/3/cb9685ru/cb9685ru.pdf (accessed on 24 May 2023).
5. About 85% of Soils in Kyzylorda Oblast Are Saline. Available online: https://eldala.kz/novosti/kazahstan/5735-v-kyzylordinskoy-oblasti-zasoleny-okolo-85-pochv (accessed on 2 May 2023).
6. Wang, J.; Ding, J.; Yu, D.; Teng, D.; He, B.; Chen, X.; Ge, X.; Zhang, Z.; Wang, Y.; Yang, X.; et al. Machine Learning-Based Detection of Soil Salinity in an Arid Desert Region, Northwest China: A Comparison between Landsat-8 Oli and Sentinel-2 MSI. *Sci. Total Environ.* **2020**, *707*, 136092. [CrossRef]
7. Fan, X.; Weng, Y.; Tao, J. Towards Decadal Soil Salinity Mapping Using Landsat Time Series Data. *Int. J. Appl. Earth Obs. Geoinf.* **2016**, *52*, 32–41. [CrossRef]
8. Qu, Y.H.; Duan, X.L.; Gao, H.Y.; Chen, A.P.; An, Y.Q.; Song, J.L.; Zhou, H.M.; He, T. Quantitative Retrieval of Soil Salinity Using Hyperspectral Data in the Region of Inner Mongolia Hetao Irrigation District. *Spectrosc. Spectr. Anal.* **2009**, *29*, 1362–1366.
9. Fallah Shamsi, S.R.; Zare, S.; Abtahi, S.A. Soil Salinity Characteristics Using Moderate Resolution Imaging Spectroradiometer (MODIS) Images and Statistical Analysis. *Arch. Agron. Soil Sci.* **2013**, *59*, 471–489. [CrossRef]
10. Taghadosi, M.M.; Hasanlou, M.; Eftekhari, K. Soil Salinity Mapping Using Dual-Polarized SAR Sentinel-1 Imagery. *Int. J. Remote Sens.* **2018**, *40*, 237–252. [CrossRef]
11. Grissa, M.; Abdelfattah, R.; Mercier, G.; Zribi, M.; Chahbi, A.; Lili-Chabaane, Z. Empirical Model for Soil Salinity Mapping from SAR Data. In Proceedings of the 2011 IEEE International Geoscience and Remote Sensing Symposium, Vancouver, BC, Canada, 24–29 July 2011.

12. Hoa, P.; Giang, N.; Binh, N.; Hai, L.; Pham, T.-D.; Hasanlou, M.; Tien Bui, D. Soil Salinity Mapping Using SAR Sentinel-1 Data and Advanced Machine Learning Algorithms: A Case Study at Ben Tre Province of the Mekong River Delta (Vietnam). *Remote Sens.* **2019**, *11*, 128. [CrossRef]
13. Ma, G.; Ding, J.; Han, L.; Zhang, Z.; Ran, S. Digital Mapping of Soil Salinization Based on Sentinel-1 and Sentinel-2 Data Combined with Machine Learning Algorithms. *Reg. Sustain.* **2021**, *2*, 177–188. [CrossRef]
14. Mohamed, S.A.; Metwaly, M.M.; Metwalli, M.R.; AbdelRahman, M.A.; Badreldin, N. Integrating Active and Passive Remote Sensing Data for Mapping Soil Salinity Using Machine Learning and Feature Selection Approaches in Arid Regions. *Remote Sens.* **2023**, *15*, 1751. [CrossRef]
15. Mukhamediev, R.I.; Popova, Y.; Kuchin, Y.; Zaitseva, E.; Kalimoldayev, A.; Symagulov, A.; Levashenko, V.; Abdoldina, F.; Gopejenko, V.; Yakunin, K.; et al. Review of Artificial Intelligence and Machine Learning Technologies: Classification, Restrictions, Opportunities and Challenges. *Mathematics* **2022**, *10*, 2552. [CrossRef]
16. Tripathi, A.; Tiwari, R.K. A Simplified Subsurface Soil Salinity Estimation Using Synergy of Sentinel-1 Sar and Sentinel-2 Multispectral Satellite Data, for Early Stages of Wheat Crop Growth in Rupnagar, Punjab, India. *Land Degrad. Dev.* **2021**, *32*, 3905–3919. [CrossRef]
17. Nurmemet, I.; Ghulam, A.; Tiyip, T.; Elkadiri, R.; Ding, J.-L.; Maimaitiyiming, M.; Abliz, A.; Sawut, M.; Zhang, F.; Abliz, A.; et al. Monitoring Soil Salinization in Keriya River Basin, Northwestern China Using Passive Reflective and Active Microwave Remote Sensing Data. *Remote Sens.* **2015**, *7*, 8803–8829. [CrossRef]
18. Guan, Y.; Grote, K.; Schott, J.; Leverett, K. Prediction of Soil Water Content and Electrical Conductivity Using Random Forest Methods with UAV Multispectral and Ground-Coupled Geophysical Data. *Remote Sens.* **2022**, *14*, 1023. [CrossRef]
19. Mukhamediev, R.I.; Symagulov, A.; Kuchin, Y.; Zaitseva, E.; Bekbotayeva, A.; Yakunin, K.; Assanov, I.; Levashenko, V.; Popova, Y.; Akzhalova, A.; et al. Review of Some Applications of Unmanned Aerial Vehicles Technology in the Resource-Rich Country. *Appl. Sci.* **2021**, *11*, 10171. [CrossRef]
20. Dorofeeva, A.; Ponomarenko, E.; Fomina, E.; Lukyanova, Y.; Buchatskiy, P. High Precision Unmanned Agro Copters In Eco-Friendly Viticulture Systems. *CEUR Workshop Proc.* **2021**, *2914*, 299–306.
21. Izmaylov, A.; Lobachevskiy, P.; Smirnov, I.; Kolesnikova, V.; Marchenko, L. Substantiation of parameters of unmanned aerial vehicles for pesticides and fertilizers application in precision farming system. *Mech. Agric. Conserv. Resour.* **2017**, *63*, 168–170.
22. Su, J.; Yi, D.; Coombes, M.; Liu, C.; Zhai, X.; McDonald-Maier, K.; Chen, W.-H. Spectral Analysis and Mapping of Blackgrass Weed by Leveraging Machine Learning and UAV Multispectral Imagery. *Comput. Electron. Agric.* **2022**, *192*, 106621. [CrossRef]
23. Bouguettaya, A.; Zarzour, H.; Kechida, A.; Taberkit, A.M. Deep Learning Techniques to Classify Agricultural Crops through UAV Imagery: A Review. *Neural Comput. Appl.* **2022**, *34*, 9511–9536. [CrossRef]
24. Castrignanò, A.; Belmonte, A.; Antelmi, I.; Quarto, R.; Quarto, F.; Shaddad, S.; Sion, V.; Muolo, M.R.; Ranieri, N.A.; Gadaleta, G.; et al. Semi-Automatic Method for Early Detection of Xylella Fastidiosa in Olive Trees Using UAV Multispectral Imagery and Geostatistical-Discriminant Analysis. *Remote Sens.* **2020**, *13*, 14. [CrossRef]
25. Benos, L.; Tagarakis, A.C.; Dolias, G.; Berruto, R.; Kateris, D.; Bochtis, D. Machine Learning in Agriculture: A Comprehensive Updated Review. *Sensors* **2021**, *21*, 3758. [CrossRef] [PubMed]
26. Kuznetsov, V.; Dmitrieva, G. *Plant Physiology*, 4th ed.; Springer Science & Business Media: New York, NY, USA, 2012; Volume 2. (In Russian)
27. Richards, L. *Diagnosis and Improvement of Saline and Alkali Soils*; Agriculture Handbook No. 60; LWW: Philadelphia, PA, USA, 1954.
28. Measuring Soil Salinity. Available online: https://www.agric.wa.gov.au/soil-salinity/measuring-soil-salinity (accessed on 3 May 2023).
29. Singh, A.N.; Dwivedi, R.S. Delineation of Salt-Affected Soils through Digital Analysis of Landsat MSS Data. *Int. J. Remote Sens.* **1989**, *10*, 83–92. [CrossRef]
30. Vermeulen, D.; Van Niekerk, A. Machine Learning Performance for Predicting Soil Salinity Using Different Combinations of Geomorphometric Covariates. *Geoderma* **2017**, *299*, 1–12. [CrossRef]
31. Gorji, T.; Yildirim, A.; Sertel, E.; Tanik, A. Remote Sensing Approaches and Mapping Methods for Monitoring Soil Salinity under Different Climate Regimes. *Int. J. Environ. Geoinform.* **2019**, *6*, 33–49. [CrossRef]
32. Sahbeni, G.; Ngabire, M.; Musyimi, P.K.; Székely, B. Challenges and Opportunities in Remote Sensing for Soil Salinization Mapping and Monitoring: A Review. *Remote Sens.* **2023**, *15*, 2540. [CrossRef]
33. Mukhamediev, R.I.; Symagulov, A.; Kuchin, Y.; Yakunin, K.; Yelis, M. From Classical Machine Learning to Deep Neural Networks: A Simplified Scientometric Review. *Appl. Sci.* **2021**, *11*, 5541. [CrossRef]
34. Yang, N.; Yang, S.; Cui, W.; Zhang, Z.; Zhang, J.; Chen, J.; Ma, Y.; Lao, C.; Song, Z.; Chen, Y. Effect of Spring Irrigation on Soil Salinity Monitoring with UAV-Borne Multispectral Sensor. *Int. J. Remote Sens.* **2021**, *42*, 8952–8978. [CrossRef]
35. Wang, D.; Chen, H.; Wang, G.; Cong, J.; Wang, X.; Wei, X. Salinity Inversion of Severe Saline Soil in the Yellow River Estuary Based on UAV Multi-Spectra. *Sci. Agric. Sin.* **2019**, *52*, 1698–1709.
36. Wei, G.; Li, Y.; Zhang, Z.; Chen, Y.; Chen, J.; Yao, Z.; Lao, C.; Chen, H. Estimation of Soil Salt Content by Combining UAV-Borne Multispectral Sensor and Machine Learning Algorithms. *PeerJ* **2020**, *8*, e9087. [CrossRef]
37. Cui, X.; Han, W.; Zhang, H.; Cui, J.; Ma, W.; Zhang, L.; Li, G. Estimating Soil Salinity under Sunflower Cover in the Hetao Irrigation District Based on Unmanned Aerial Vehicle Remote Sensing. *Land Degrad. Dev.* **2022**, *34*, 84–97. [CrossRef]

38. Zhu, C.; Ding, J.; Zhang, Z.; Wang, Z. Exploring the Potential of UAV Hyperspectral Image for Estimating Soil Salinity: Effects of Optimal Band Combination Algorithm and Random Forest. *Spectrochim. Acta Part A Mol. Biomol. Spectrosc.* **2022**, *279*, 121416. [CrossRef]
39. Zhang, Z.; Niu, B.; Li, X.; Kang, X.; Wan, H.; Shi, X.; Li, Q.; Xue, Y.; Hu, X. Inversion of soil salinity in China's Yellow River Delta using unmanned aerial vehicle multispectral technique. *Environ. Monit. Assess.* **2023**, *195*, 245. [CrossRef]
40. Hu, J.; Peng, J.; Zhou, Y.; Xu, D.; Zhao, R.; Jiang, Q.; Fu, T.; Wang, F.; Shi, Z. Quantitative Estimation of Soil Salinity Using UAV-Borne Hyperspectral and Satellite Multispectral Images. *Remote Sens.* **2019**, *11*, 736. [CrossRef]
41. Dwivedi, A.K.; Singh, A.K.; Singh, D. An Object Based Image Analysis of Multispectral Satellite and Drone Images for Precision Agriculture Monitoring. In Proceedings of the IGARSS 2022—2022 IEEE International Geoscience and Remote Sensing Symposium, Kuala Lumpur, Malaysia, 17–22 July 2022.
42. Xie, L.; Feng, X.; Zhang, C.; Dong, Y.; Huang, J.; Cheng, J. A Framework for Soil Salinity Monitoring in Coastal Wetland Reclamation Areas Based on Combined Unmanned Aerial Vehicle (UAV) Data and Satellite Data. *Drones* **2022**, *6*, 257. [CrossRef]
43. Dindaroğlu, T.; Kılıç, M.; Günal, E.; Gündoğan, R.; Akay, A.E.; Seleiman, M. Multispectral UAV and Satellite Images for Digital Soil Modeling with Gradient Descent Boosting and Artificial Neural Network. *Earth Sci. Inform.* **2022**, *15*, 2239–2263. [CrossRef]
44. Zhang, Z.; Niu, B.; Li, X.; Kang, X.; Hu, Z. Estimation and Dynamic Analysis of Soil Salinity Based on UAV and Sentinel-2a Multispectral Imagery in the Coastal Area, China. *Land* **2022**, *11*, 2307. [CrossRef]
45. Agricultural Drone Mapping: Crop Protection and Production. Available online: https://www.pix4d.com/industry/agriculture (accessed on 3 May 2023).
46. Khan, N.; Rastoskuev, V.; Shalina, E.; Sato, Y. Mapping Salt-Affected Soils Using Remote Sensing Indicators—A Simple Approach with the Use of GIS IDRISI. In Proceedings of the 22nd Asian Conference on Remote Sensing, Singapore, 5–9 November 2001.
47. Bannari, A.; Guedon, A.M.; El-Harti, A.; Cherkaoui, F.Z.; El-Ghmari, A. Characterization of Slightly and Moderately Saline and Sodic Soils in Irrigated Agricultural Land Using Simulated Data of Advanced Land Imaging (EO-1) Sensor. *Commun. Soil Sci. Plant Anal.* **2008**, *39*, 2795–2811. [CrossRef]
48. Abbas, A.; Khan, S. Using Remote Sensing Techniques for Appraisal of Irrigated Soil Salinity. In Proceedings of the International Congress on Modelling and Simulation (MODSIM), Christchurch, New Zealand, 10–13 December 2007; pp. 2632–2638.
49. Tripathi, N.; Rai, B.; Dwivedi, P. Spatial Modeling of Soil Alkalinity in GIS Environment Using IRS Data. In Proceedings of the 18th Asian Conference on Remote Sensing, Kuala Lumpur, Malaysia, 20–24 October 1997.
50. Douaoui, A.E.; Nicolas, H.; Walter, C. Detecting Salinity Hazards within a Semiarid Context by Means of Combining Soil and Remote-Sensing Data. *Geoderma* **2006**, *134*, 217–230. [CrossRef]
51. Khan, N.M.; Rastoskuev, V.V.; Sato, Y.; Shiozawa, S. Assessment of Hydrosaline Land Degradation by Using a Simple Approach of Remote Sensing Indicators. *Agric. Water Manag.* **2005**, *77*, 96–109. [CrossRef]
52. Tivianton, T.A.; Kurnia, R. Detection of Cropland Salinization with Vegetation Index in Various Coastal Condition. *IOP Conf. Ser. Earth Environ. Sci.* **2019**, *256*, 012051. [CrossRef]
53. Yu, X.; Chang, C.; Song, J.; Zhuge, Y.; Wang, A. Precise Monitoring of Soil Salinity in China's Yellow River Delta Using UAV-Borne Multispectral Imagery and a Soil Salinity Retrieval Index. *Sensors* **2022**, *22*, 546. [CrossRef] [PubMed]
54. Weiss, K.; Khoshgoftaar, T.M.; Wang, D.D. A Survey of Transfer Learning. *J. Big Data* **2016**, *3*, 9. [CrossRef]
55. Friedman, J.H. Greedy Function Approximation: A Gradient Boosting Machine. *Ann. Stat.* **2001**, *29*, 1189–1232. [CrossRef]
56. Chen, T.; Guestrin, C. XGBoost. In Proceedings of the 22nd ACM SIGKDD International Conference on Knowledge Discovery and Data Mining, San Francisco, CA, USA, 13–17 August 2016.
57. Ke, G.; Meng, Q.; Finley, T.; Wang, T.; Chen, W.; Ma, W.; Ye, Q.; Liu, T. LightGBM: A Highly Efficient Gradient Boosting Decision Tree. *Adv. Neural Inf. Process. Syst.* **2017**, *30*, 3149–3157.
58. Daoud, E. Comparison between XGBoost, LightGBM and CatBoost Using a Home Credit Dataset. World Academy of Science, Engineering and Technology, Open Science Index 145. *Int. J. Comput. Inf. Eng.* **2019**, *13*, 6–10.
59. Bentéjac, C.; Csörgő, A.; Martínez-Muñoz, G. A Comparative Analysis of Gradient Boosting Algorithms. *Artif. Intell. Rev.* **2020**, *54*, 1937–1967. [CrossRef]
60. Breiman, L. Random forests. *Mach. Learn.* **2001**, *45*, 5–32. [CrossRef]
61. Cortes, C.; Vapnik, V. Support-Vector Networks. *Mach. Learn.* **1995**, *20*, 273–297. [CrossRef]
62. Yu, H.-F.; Huang, F.-L.; Lin, C.-J. Dual Coordinate Descent Methods for Logistic Regression and Maximum Entropy Models. *Mach. Learn.* **2010**, *85*, 41–75. [CrossRef]
63. Santosa, F.; Symes, W.W. Linear Inversion of Band-Limited Reflection Seismograms. *SIAM J. Sci. Stat. Comput.* **1986**, *7*, 1307–1330. [CrossRef]
64. Tichonov, A.N. *Numerical Methods for the Solution of Ill-Posed Problems*; Kluwer: Dordrecht, The Netherlands, 1995.
65. Hoerl, A.E.; Kennard, R.W. Ridge Regression: Applications to Nonorthogonal Problems. *Technometrics* **1970**, *12*, 69–82. [CrossRef]
66. Zou, H.; Hastie, T. Regularization and Variable Selection via the Elastic Net. *J. R. Stat. Soc. Ser. B (Stat. Methodol.)* **2005**, *67*, 301–320. [CrossRef]
67. Mukhamediev, R.I.; Kuchin, Y.; Amirgaliyev, Y.; Yunicheva, N.; Muhamedijeva, E. Estimation of Filtration Properties of Host Rocks in Sandstone-Type Uranium Deposits Using Machine Learning Methods. *IEEE Access* **2022**, *10*, 18855–18872. [CrossRef]
68. Raschka, S. MLxtend: Providing Machine Learning and Data Science Utilities and Extensions to Python's Scientific Computing Stack. *J. Open Source Softw.* **2018**, *3*, 638. [CrossRef]

69. Raschka, S. Available online: https://rasbt.github.io/mlxtend/ (accessed on 3 May 2023).
70. Zhao, W.; Zhou, C.; Zhou, C.; Ma, H.; Wang, Z. Soil Salinity Inversion Model of Oasis in Arid Area Based on UAV Multispectral Remote Sensing. *Remote Sens.* **2022**, *14*, 1804. [CrossRef]
71. What Is the Center Wavelength and Bandwidth of Each Filter for MicaSense-Sensors. Available online: https://support.micasense.com/hc/en-us/articles/214878778 (accessed on 3 May 2023).